Smart Structures and Systems, Vol. 5, No. 6 (2009) 645-662
DOI: http://dx.doi.org/10.12989/sss.2009.5.6.645

Ni-Ti actuators and genetically optimized compliant ribs for an adaptive wing

Giuseppe Mirone

Dipartimento di Ingegneria Industriale e Meccanica, University of Catania
Viale A. Doria 6, 95125 Catania, Italy

(Received November 27, 2007, Accepted March 24, 2009)

Abstract. Adaptive wings are capable of properly modifying their shape depending on the current aerodynamic conditions, in order to improve the overall performance of a flying vehicle. In this paper is presented the concept design of a small-scale compliant wing rib whose outline may be distorted in order to switch from an aerodynamic profile to another. The distortion loads are induced by shape memory alloy actuators placed within the frame of a wing section whose elastic response is predicted by the matrix method with beam formulation. Genetic optimization is used to find a wing rib structure (corresponding to the first airfoil) able to properly deforms itself when loaded by the SMA-induced forces, becoming as close as possible to the desired target shape (second airfoil). An experimental validation of the design procedure is also carried out with reference to a simplified structure layout.

Keywords: shape memory alloy; SMA actuator; adaptive wing; compliant structure; genetic algorithm.

1. Introduction

Each wing is designed as the best possible compromise for the given set of flight conditions which the vehicle is expected to experience in its operating life. But the performance of a wing is usually optimized for a single subset of aerodynamic parameters and decays more or less rapidly as the current flight conditions deviate from the optimal design ones. Then, a desirable feature of every wing is the capability of adapting its own shape to continuously varying aerodynamic parameters (Gandhi and Anusonti-Inthra 2008, Lim, *et al*. 2005, Neal, *et al*. 2004, Strelec, *et al*. 2002, 2003, Garner, *et al*. 2000); to some extents this can be accomplished in conventional wings by way of various aerodynamic devices like spoilers, ailerons, aerobrakes etc.

All the latter systems induce discontinuities, edges and gaps in the wing surfaces, resulting in considerable loss of the wing efficiency, so that margins for large improvements in the overall aerodynamic performance can be attained if continuous and gap-free shape modifications are imposed to the wing (Lim, *et al*. 2005, Campanile and Anders 2005, Monner 2001, Stanewsky 2000).

The deformations corresponding to meaningful changes in an airfoil are compatible with the large reversible strains typical of shape memory alloys (SMA), so that these metals can be used to realize an entirely active wing (structure and/or external surface), but current research is mostly aimed at coupling SMA actuators to compliant wing structures (Shili, *et al.* 2008, Mirone 2007, Raja, *et al.* 2006,

*E-mail: gmirone@diim.unict.it

Waisman and Abramovich 2004, Campanile, *et al.* 2000, Bein, *et al*. 2000); in fact, the reduced weight, dimensions and the amount of energy per unit mass these actuators are capable of (Song and Ma 2007, Tanaka and Sanada 2007, Syaifuddin, *et al.* 2006, Elzey, *et al*. 2005, Huang 2002, Icardi 2001) are very promising.

In this paper is presented the design of the adaptive wing for a small unmanned aerial vehicle or UAV (Vos, *et al.* 2007, Neal, *et al*. 2004, Pettit, *et al.* 2001, Van Blyenburgh 1999), in the wingspan range 1-5 meters.

A single wing rib is considered in this study, its internal topology and geometric parameters being determined by way of a genetic algorithm (Schmitt 2001, Vose 1999, Whitley1994) devoted to achieving that, under the action of prescribed actuation loads, the external contour of the wing rib passes from an undeformed state corresponding to the NACA M6 airfoil, to a deformed state reproducing as closely as possible the NACA M27 airfoil.

The actuators are made of one-way NiTi wires coupled to helicoidal springs in order to forcing the wires to return at their pre-elongated state each time the joule heating is stopped and the austenitic-martensitic phase change is completed.

Experimental tests on NiTi wires are conducted for characterizing the alloy by determining its stress-strain-temperature relationship and its transformation temperatures (Azadi, *et al*. 2006, Kato, *et al*. 2004, Brocca, *et al*. 2002, Govindjee and Garrett 2000, Auricchio and Sacco 1999), so that the successive design of the actuators may be carried out by finding the right coupling between structure stiffness, spring stiffness, wire length and pre-strain.

The SMA-actuated wing rib then is realized, and its accuracy in reproducing the desired shape modifications is assessed by image analysis techniques.

2. SMA characterization

The shape memory alloy wires used for this work have a diameter of 1.27 mm and are made of high-temperature NiTi; the heating required for the martensite-austenite phase change is supplied by joule effect and the temperature measurements are performed by way of an AGEMA THV 900 infrared camera.

Temperature measurements by infrared radiation are based on the knowledge of the emissivity of the surface whose temperature has to be measured, so the first set of experiments aimed at determining the emissivity of the wire.

A length of wire, partially covered with mat black paint to achieve an emissivity of 0.95 over half of its length, is fed with direct current and a stabilized infrared image of the heated wire is acquired after a transitory time of about 20 seconds. The emissivity of the infrared analyzer is set to 0.95 so that the reading gives the real temperature of the black-painted wire, then the analyzer emissivity is adjusted until the same temperature reading is obtained on the un-painted half of the wire.

This procedure, repeated for different values of the feeding current, allows to determine the current-temperature relationship in Fig. 1 (room temperature *Tenv*=21 ^{o}C) and the temperature-emissivity relationship in Fig. 2. If *Tenv* does not deviate much from 21 C, the quadratic best fit polynomial can be still used by imposing that the zero-order constant equals *Tenv.*

The relationship in Fig. 1 expresses the equilibrium temperature achieved after different amounts of time, depending on how the whole current evolves in time. Anyway the time for reaching the equilibrium temperature can be easily controlled electronically, in fact a closed-loop control system can initially

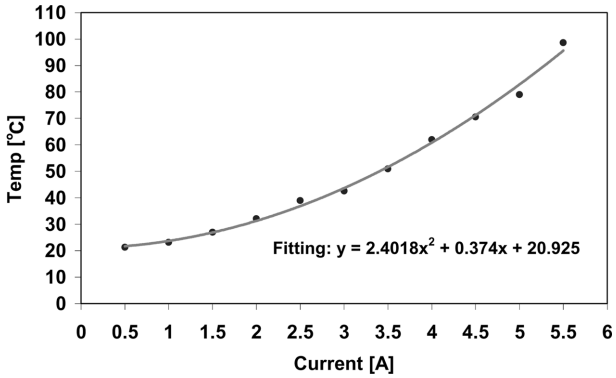

Fig. 1 Temperature vs. feeding current

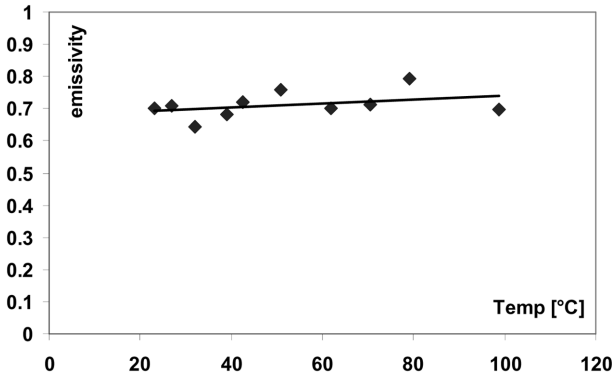

Fig. 2 Emissivity vs. temperature

supply a current as intense as desired for accelerating the temperature rise, then, when the temperature approaches the desired value, the control system can gradually reduce the current up to the regime value corresponding to the desired point in Fig. 1. Ideally, a current impulse of very large amplitude maintained for a very short time, followed by the opportune constant current, could allow to achieve almost instantaneously the temperatures according to the curve in Fig. 1.

The emissivity has only slight variations in the temperature range investigated, so the average value of 0.71 is assumed as a constant for the successive calculations.

The transformation temperatures are then determined by performing cyclical elongation vs. temperature tests under constant load, whose results are visible in Figs. 3 and 4 for the constant stress levels of 40, 56 and 80 MPa.

Operating temperatures for aircraft structures are extremely variable, but problems with the one-way shape memory alloy used here may arise mainly from high temperatures; in fact, the altitude-induced low temperature may only require that the control system delivers more electric power for heating the wires and accelerates the cooling when current is reduced or removed, so low external temperatures do not affect the overall functionality of the actuators.

On the contrary, temperatures in the range 50-100 C due to hot climate at low altitude and solar radiation over metal structures, may cause unwanted phase change of the alloy as far as the wires heating cannot be easily contrasted by artificial cooling: this means that the alloy described here could be only used at external temperatures below 40 °C. A practical solution for overcoming the effect of

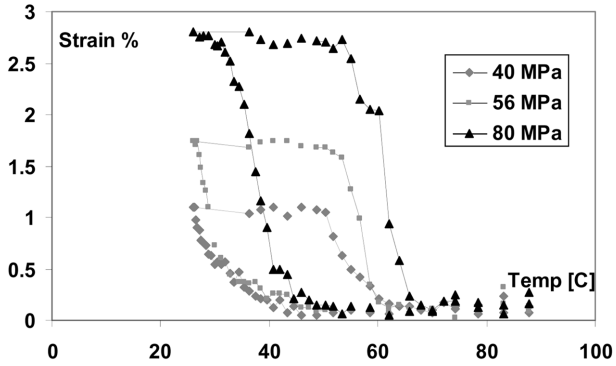

Fig. 3 Strain-temperature cycles at constant load

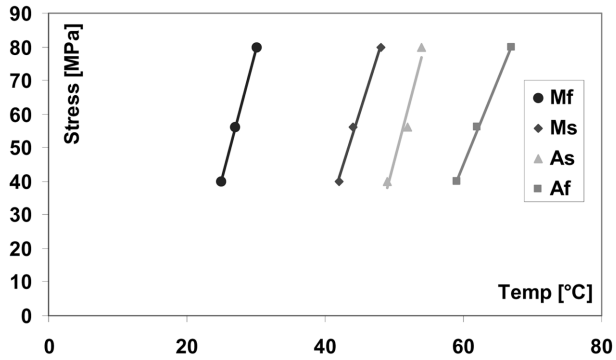

Fig. 4 Transformation temperatures vs. stress

natural heating is that of using shape memory alloys of the higher temperature type, having « Austenite start » temperatures beyond 100 C, while a more complex but refined solution for using these SMA could consists of using a cooling system for completely controlling the temperature of wires by active cooling and active heating.

The stress-strain curves are then determined by performing tensile tests on NiTi wires heated at different constant temperatures, as reported in Figs. 5 and 6 where it is visible that, despite some load oscillations at the intermediate temperatures, all the curves up to the end of the plateau can be adequately fit by piecewise linear functions.

Most probably the oscillations occur because the stress-induced martensite transformation of NiTi implies latent heat exchange and modifications in the material thermal parameters, while the joule heating at constant current is not able to quickly compensate with increasing or decreasing amperage for maintaining a rigorously constant temperature.

By heating the unloaded wires after each tensile test is determined the recoverable strain represented by the distance between the two triangular points on the horizontal axes of each plot in Figs. 5 and 6. The amount of eventually un-recovered strain indicates that the yield point on the martensitic stress-strain curve has been exceeded. The resulting maximum recoverable strain is close to 4.1%, and an unloading ramp passing for the point (0.041,0) on the stress-strain plane, intersects the martensitic curve at a strain of 0.047 and a stress of 180 MPa, these representing the yield conditions.

In Fig. 7 is reported the complete set of experimental curves from the tensile tests, together with a

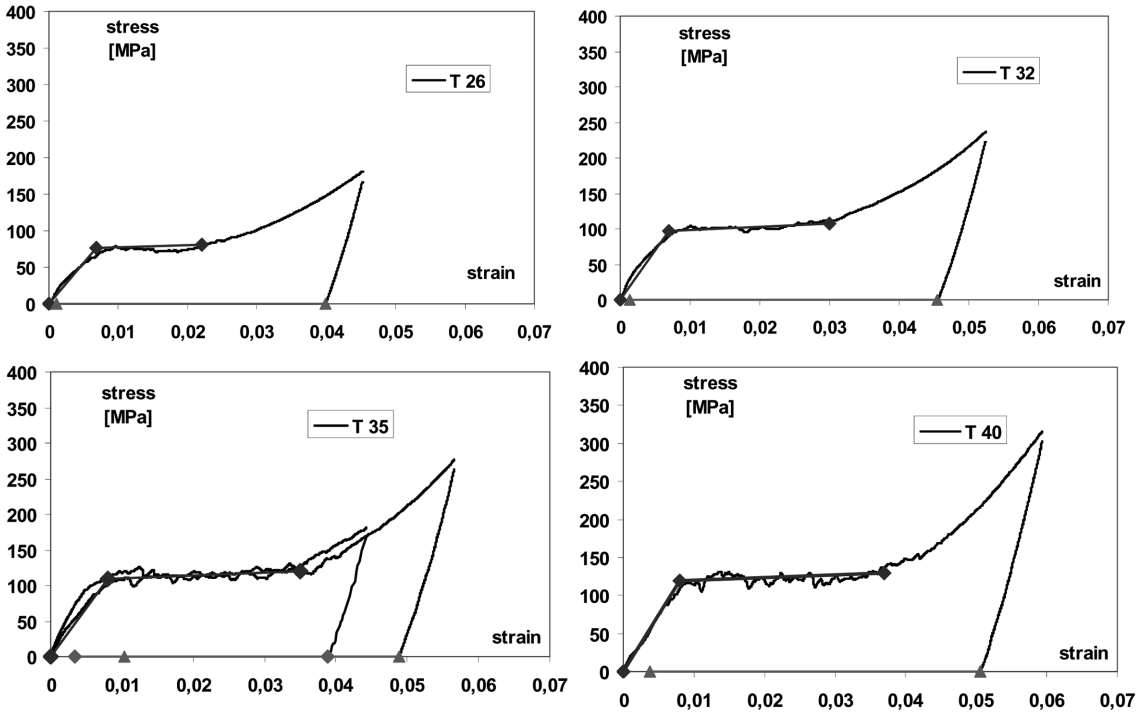

Fig. 5 Stress-strain curves at 26, 32, 35 and 40 °C

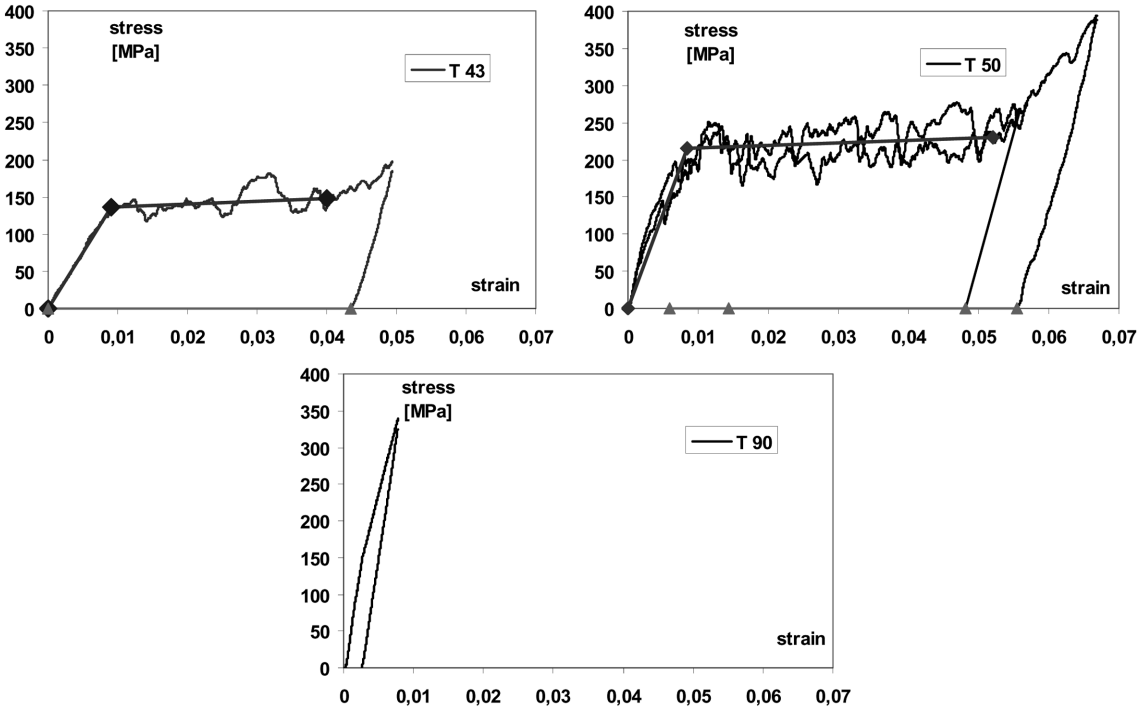

Fig. 6 Stress-strain curves at 43, 50 and 90 °C

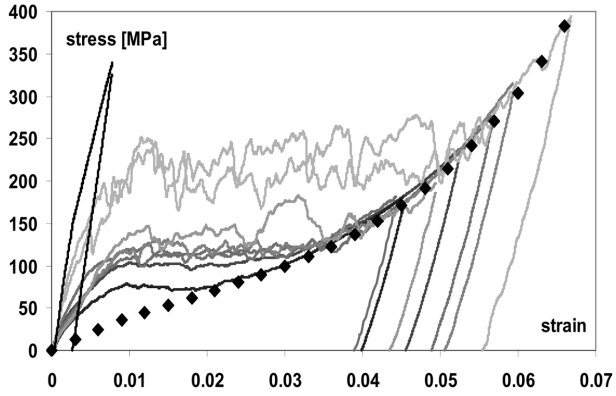

Fig. 7 Experimental curves and post-plateau stress-strain behavior

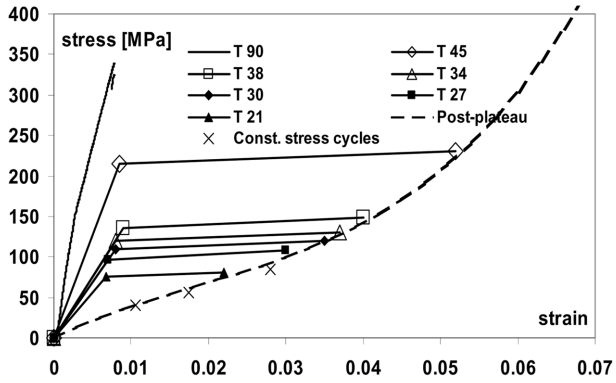

Fig. 8 Simplified stress-strain curves at different temperatures

diamond-dotted curve representing the cubic best fitting function which seems to well approximate the post-plateau behavior of NiTi at all the temperatures examined.

Given the reasonable accuracy of the cubic best fit in reproducing all the post-plateau curves, in the following sections of the paper the entire set of stress-strain data is more easily handled by adopting the bilinear approximations up to each plateau end and the cubic approximation beyond the plateau. The final form of the stress-strain data to be used for the design of actuators is shown in Fig. 8 without the unloading ramps; three stress-strain points obtained from the temperature-strain cycles at constant load are also reported there as x-shaped markings.

The elastic moduli are estimated from the stress-strain curves by accounting for the stiffness of the Instron testing machine. Stress and strains between 50 and 100 MPa on the loading ramp of the austenitic NiTi at 90 C at indicate an elastic modulus of about 72 Gpa, while, for the fully martensitic state, the modulus is calculated from the unloading ramps and results close to 34 GPa.

3. Actuators modeling

The desired effect of the SMA actuator is that of deforming the elastic wing rib when the wire contracts due to heating, while, after cooling, the wire must elongate in order to restore the initial shape

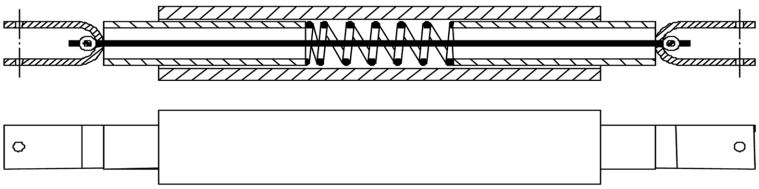

Fig. 9 Actuators layout

of the rib frame.

Due to the one-way shape memory behavior of the alloy selected, the original elongation of the martensitic wire after cooling must be restored by an external load which, in this case, is supplied by the combined elastic reaction of the wing rib frame and that of an actuator spring. A scheme of the assembled actuator is reported in Fig. 9.

The first input data for the design of each actuator is the required stroke DL, determined by the positions of the actuator attachments to the wing rib in the undeformed frame (NACA M6 airfoil) and in the deformed frame (best possible approximation of the NACA M 27 airfoil).

The stress-strain curves of NiTi are then transformed into Displacement-Load curves by for given values of the wire cross section and of its unstrained length.

The undeformed frame rib machined with the shape of the M 6 airfoil corresponds to the fully elongated actuators (martensitic wires), while the deformed frame in the M27 configuration corresponds to the contracted actuators (austenitic wires), loaded by the elastic reactions of spring and frame.

The NiTi wires coupled to the spring and the elastic rib structure constitute a system whose mechanical behaviour can be described by the set of equations described ahead in this chapter and by a Load-Elongation chart like that of Fig. 10.

Given the required wire elongation between martensite and austenite (actuator stroke, double-pointed arrows in Fig. 10), the initial length L_0 of the unloaded austenitic wire (needed for translating strains into wire elongations DL) and the stiffness of the compliant structure, a free mathematical parameter remains to be constrained for determining the actuator working points on the Load-Displacement plane.

In Fig. 10 are shown the characteristics of three different actuators capable of the same stroke between the points *Ai* and *Mi*.

The dash-dotted segments *Ai-Mi* define the characteristic of the elastic reaction from the spring and

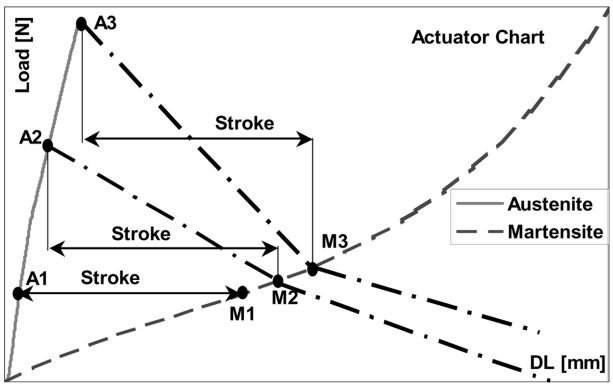

Fig. 10 Typical actuator chart

the structure, needed to restore the martensitic elongation of each actuator after its cooling.

The *A1-M1* segment represents the limit case of an actuator which ideally should work against a constant-valued opposing load, and the other limit position *A3-M3* corresponds to the yield stress of the martensitic NiTi;

In order to restore the shape of the M6 airfoil in the martensitic state, the total force elongating a wire must be induced by two elastic reactions, the first due to the wing rib and the second due to a compressed spring within the actuator. When the wire is elongated up to *Mi* in the martensitic phase, the elastic reaction of the airfoil frame vanishes because the whole frame is undeformed, so that the only remaining force equilibrating the residual wire traction at the *Mi* point is due to the actuator spring. When the wire contracts due to heating, the equilibrium point moves toward *Ai*, the elastic frame is deformed and the total force opposing the wire contraction is given by both the spring and the frame elastic reactions. In other words, the actuator spring is preloaded to equilibrate the tensile stress of the martensitic wire in the *Mi* state, when the wing rib structure must be unloaded and undeformed.

Then the inclination of segments *Ai-Mi* expresses the combined stiffness of the spring and the frame in parallel, while the segment below *Mi* expresses the stiffness of the actuator spring alone.

The design procedure, typically leading to charts like that in Fig. 10, derives from the following mathematical model.

Stress-strain functions as those plotted in Fig. 8 must be preliminarily determined for the austenitic and the martensitic wires, $\sigma_A(\varepsilon)$ and $\sigma_M(\varepsilon)$ respectively.

The length of the actuator wire in the fully extended (L_M) and fully retracted configuration (L_A) is defined depending on the position chosen for the points where the actuator is attached to the compliant wing rib frame. The required actuator stroke is simply obtained as their difference:

$$Stroke = L_M - L_A \tag{1}$$

The choice of the attachment points and the corresponding actuator stroke must be compatible with the maximum elongation of which NiTi is capable, 4% in our case. The maximum working stress σ_A^* of the austenitic wire can be set at whatever value below the austenitic yield stress, then the corresponding strain ε_A^* must be determined from the function $\sigma_A(\varepsilon)$; then the length of the undeformed wire L_0 can be calculated as in Eq. (2), together with the required elongation ΔL_A of the loaded austenitic wire:

$$\begin{gathered} \varepsilon_A^* = \varepsilon_A(\sigma_A^*) \\ \begin{cases} \varepsilon_A^* = \dfrac{\Delta L_A}{L_0} \\ L_A = L_0 + \Delta L_A \end{cases} \Rightarrow \begin{cases} L_0 = \dfrac{L_A}{1+\varepsilon_A^*} \\ \Delta L_A = \varepsilon_A^* \cdot \dfrac{L_A}{1+\varepsilon_A^*} \end{cases} \end{gathered} \tag{2}$$

Said ΔL and S the generic wire elongation and the cross sectional area respectively, the stress-strain functions can be expressed in terms of force-elongation as in Eq. (2):

$$\begin{aligned} F_A(\Delta L) &= \sigma_A\left(\frac{\Delta L}{L_0}\right) \cdot S \\ F_M(\Delta L) &= \sigma_M\left(\frac{\Delta L}{L_0}\right) \cdot S \end{aligned} \tag{3}$$

so that by Eqs. (2), (3) and the known value of L_M, the three remaining coordinates of the points A and M of Fig. 10 can be determined:

$$\Delta L_M = L_M - L_0$$
$$F_M^* = F_M(\Delta L_M) = \sigma_M\left(\frac{\Delta L_M}{L_0}\right) \cdot S$$
$$F_A^* = F_A(\Delta L_A) = \sigma_A\left(\frac{\Delta L_A}{L_0}\right) \cdot S \tag{4}$$

To ensure that yielding does not occur in the martensitic state, must be verified that

$$\Delta L_M \leq 4\% \cdot L_0 \tag{5}$$

The slope of the segment A-M is the total stiffness K_T of the airfoil frame (K_F) in parallel to the actuator spring (K_S):

$$K_T = K_F + K_S = \frac{F_A^* - F_M^*}{Stroke} \tag{6}$$

The subdivision of K_T in K_F and K_S clearly influences the load subdivision between the frame and the spring; K_T can be split into its component according to various criteria, in this case the choice of the two stiffnesses composing K_T is made by setting the maximum stress ooccurring on the frame, as expressed in Eq. (7):

$$K_F = \frac{F_F}{Stroke}$$
$$K_S = K_T - K_F \tag{7}$$

The first equation in Eq. (7) ensures that, after deformation, the desired shape is obtained in the zones where actuators are attached; then the genetic algorithm which finds the frame shape must comply with this stiffness requirement.

4. Genetic approach to the wing rib design

NACA M6 and NACA M27 airfoils are selected for this application because they are suitable for flight at low Reynolds numbers (small vehicles at low speed) and have almost the same thickness/chord ratio, as visible in Fig. 10 where the two profiles are plotted at a dilated vertical scale for better exploiting their shapes.

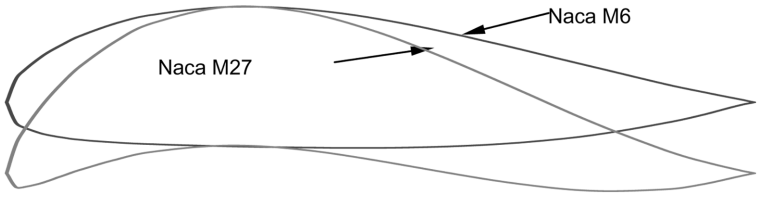

Fig. 11 Selected airfoils

The intersections between the two airfoils are taken as the most convenient locations for the attachments to the wing spars, given that here the wing has its maximum thickness.

The coupling of a Genetic Algorithm (G.A.) with the beam matrix method formulation allows to search for a frame outlined as the M6 profile which, deformed under the action of the F_F loads, approximates the M27 profile.

A wing spar frame is defined by the coordinates of its nodes and by a binary string containing the set of the in-plane thickness values for each node-to-node beam, the out-of-plane thickness being held constant for the entire structure.

While the coordinates of each node of the undeformed configuration are not modified within the G.A., the in-plane thickness of each beam is allowed to vary within a specified range, where a null thickness means that a beam is removed from the structure.

A starting population of ten frames, all having the same nodes but differently assorted thicknesses, is generated by randomly assigning admissible values to the thickness of each beam in a frame.

All frames of the starting population are subjected to the F_F loads and their deformed contour, calculated by the matrix method with beam formulation, is compared to the desired shape of the M 27 airfoil.

The "De Jong 1" objective function, available in a Matlab package for genetic algorithms, is evaluated by defining a vector containing the squared distances between the contour nodes and the M 27 target profile as well as the squared difference between an imposed limit stress σ_L and the maximum stress on that frame.

The lower value of the objective function among the current ten-frames population is extracted for indicating the performance achieved by that generation, then the procedure for generating a new population takes place.

A ranking, based on assigning a fitness value to each individual, is made for the current parental population which then generates a population of offsprings through the application of selective, crossover and mutational operators.

The lower is the objective function of a frame, the higher is its fitness function which, in turn, influences the probability of being selected for generating the successive population of frames.

From the i^{th} population, the better performing individuals are selected by the roulette method, recombined by crossover, modified by mutation operators and then substituted to the worst frames of the i^{th} population, so generating the $(i+1)^{th}$ population.

The topology of each frame is partially defined by the initial frame because no new beams are defined by the genetic algorithm, but some of the existing ones may be deleted by imposing null thickness; then the maximum number of beams *NBmax* is an imposed design data. Further constraints are set to the size of each population (N=10), the thickness of the beams ($0 < t < t_{max}$), to the generational gap determining how many individuals of the current generation are selected for being transformed (ggap = 0.9), recombined by mixing their chromosomes with those of a certain percentage of the parental population (gcross = 0.7) and mutated by modifying some of the resulting thickness values.

If the convergence criterion is met (the objective function is addressed within a specified tolerance), no further populations will be generated and the solution proposed by the G.A. is the better among those already generated when the stop condition occurs, otherwise the procedure is stopped at the $maxgen^{th}$ iteration. Further runs can then be launched by using the $maxgen^{th}$ population generated in the previous not-converging run as the initial population of a new run.

In our case, the adoption of the limit stress of 30 MPa in defining the objective function together with the M27 airfoil shape, means that the ideal wing frame must deform as required and, at the same time,

must also undergo an uniform stress equal to σ_L.

For bending beams this is impossible by definition, so the inclusion of σ_L in the objective function has only the role of making the stress as uniform as possible for the given structure, accepting a priori that the complete uniformity may not be achieved. This implies that the values of the objective function may never vanish and are not representative in a practical sense of how a structure is close to the desired one, so it is not easy to set a reasonable tolerance value for ending the iterative algorithm.

Given these considerations, no specified value of the objective function is set in our case for stopping the algorithm, but the constraint parameter *maxgen* is set to 100; in many consecutive runs performed it turned out that, well before the 100^{th} iteration, the objective function stabilized at a value which, given the nature of G.A., indicates that the minimum is found for the objective function over the given range of constrained variables. The main advantage of genetic algorithms for optimization problems, with respect to gradient-based algorithms, is their quickness in finding an approximate but reasonable solution; as a counterpart to their flexibility, G.A. may lead to suboptimal solutions, meaning that they are prone to the risk of locking at a local minimum. This can be alleviated thanks to the partially randomized nature of the mutations and of the generating process G.A. are based on, but the certainty of locating absolute minima in the selected range of variables is not achievable.

5. Frame and actuators design

A plate of Nylon 66 (elastic modulus 2000 MPa), 21 mm thick, is used as reference for realizing the compliant wing rib demonstrator given its good balance between strength and elasticity.

The first frame layout analyzed is obtained by subdividing the inner area within an M6 airfoil of 600 mm chord in rectangular cells as shown in Fig. 12.

The out-of-plane length of the rib is 21 mm. The in-plane thickness of the beams of the external profile is held at 1 mm, while the thickness of each inner member of the frame is allowed to vary in the discrete set [0; 0.2; 0.3; 0.4; 0.5; 0.6; 0.7; 0.8] mm.

The placement of NiTi wires, represented by the dashed red lines, is based on the consideration that such an arrangement is compatible with anchoring the actuators to the stiffer part of the wing section (attachments close to the center spar in the area of maximum profile thickness), and enables to pulling downward the leading and trailing edges for increasing the profile camber, as required for deforming the M6 airfoil toward the M27 one.

According to the results of some preliminary finite elements analyses, the F_F fraction of the total actuator force which must be carried by the frame is set to 20 N for the actuator on the trailing edge and 30 N for that on the stiffer leading edge, for preventing any overstress of the cellular nylon structure.

After 100 iterations, the optimized frame thickness distribution suggested by the G.A. is that depicted in Fig. 13(a) (M6 profile), which allows to reproduce the desired shape of the M27 airfoil by deforming

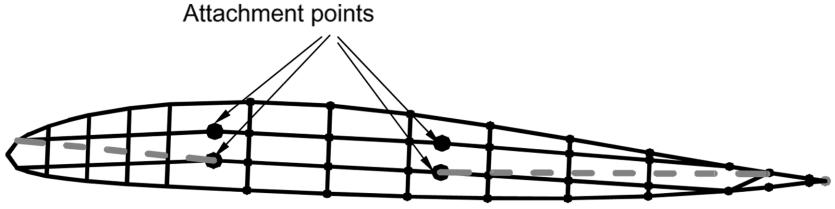

Fig. 12 Wing rib layout # 1

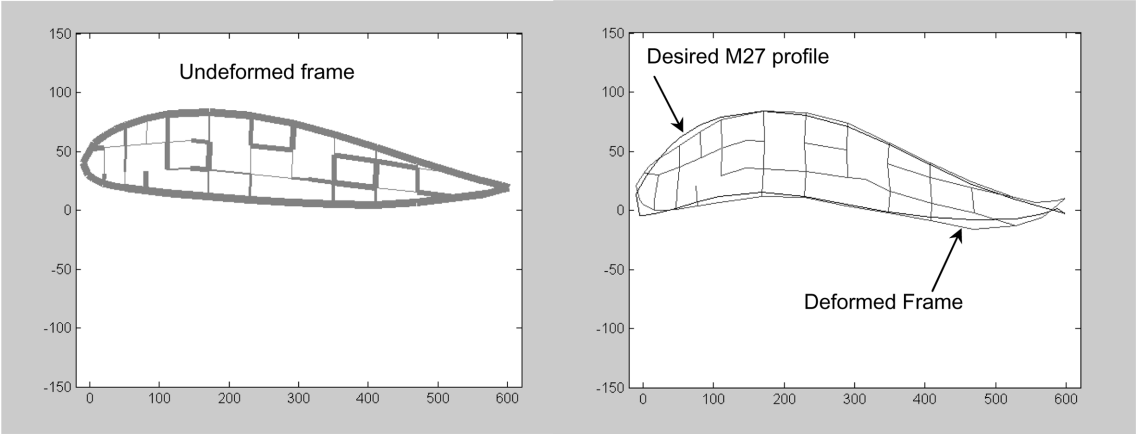

Fig. 13 Genetically evolved frame, undeformed (thickness) and deformed

Table 1 Actuator parameters

	Actuator # 1	Actuator # 2
σ_A^* [Mpa]	300	300
ε_A^*	0.0067	0.0067
L_A [mm]	143.1	271.8
L_M [mm]	145	275.8
F_F [N]	20	30
L_0 [mm]	142.1	270
F_A^* [N]	380	380
F_M^* [N]	85.6	90.7
K_T [N/mm]	158.6	74.3
K_S [N/mm]	148	67
Preload [mm]	0.6	1.4

as in Fig. 13(b).

Some missing beams are visible with respect to Fig. 12 (including one converging at a rib-spar attachment points), this indicating that the algorithm assigns them null thickness.

The maximum stress on the frame is 26.9 MPa, and the average distance between the deformed profile and the desired one is 0.9 mm with a maximum distance close to 12 mm, in the lower contour near the trailing edge. Actuators data and design parameters from Eqs. (1)-(7) are reported in Table 1, while the actuators characteristics are plotted in Fig. 14.

By including the position of internal nodes, the position of the actuators attachments and the magnitude of the actuation loads among the genetically optimized parameters could result in substantial improvement of the wing design, but the great increase of complexity required for such a degree of detail is beyond the demonstrative scope of this work.

The same above procedure is carried out for designing a wing rib and its actuators with reference to the frame topology defined as in Fig. 15, where the area within the profile is not crossed by any beam except for a central zone where a full-height solid spar supports and stiffens the wing rib. This simplified structure is intended for validating purposes, so that a prototype of the wing rib with

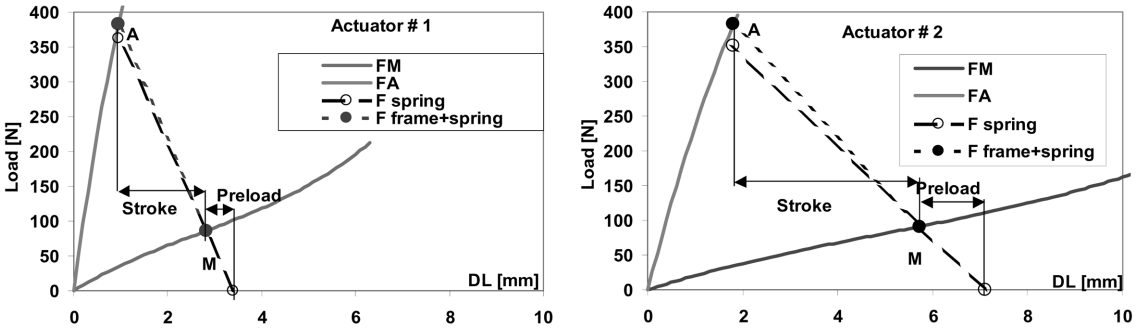

Fig. 14 Actuators diagrams

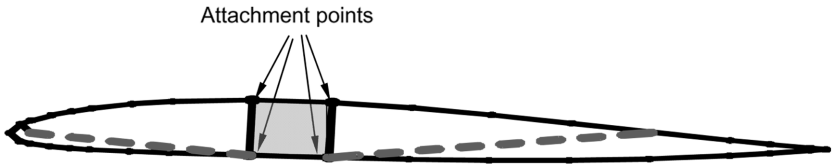

Fig. 15 Wing rib layout # 2

actuators can be more easily realized and experimentally tested, its response being then compared to the predicted one.

The airfoil profile is segmented in 36 beams, each of thickness varying in the set [2, 3, 4, 5] mm, now being clearly impossible to suppress any beam by reducing its thickness to zero.

Of the total load acting on each SMA wire, the fraction F_F contrasted by the frame elastic reaction is set to 50 N and 30 N, for the leading edge and the trailing edge actuators, respectively. Greater loads than the previous application are used now, in order to avoid too thin beams which could require too precise machining of the nylon frame.

Again, a sounding value of the objective function for stopping the algorithm cannot be estimated a priori and, after 80 iterations of the G.A., only minor improvements can be obtained by successive generations in reproducing the desired M27 shape, so the better frame of the 100th population is taken as the final result.

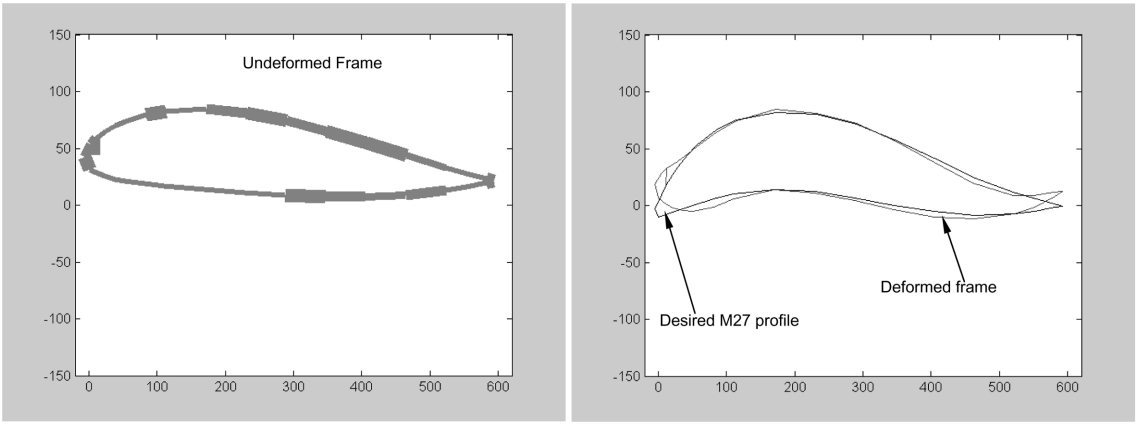

Fig. 16 Genetic evolution of the frame # 2, undeformed and deformed

Table 2 Actuator parameters for frame # 2

	Actuator # 1	Actuator # 2
σ_A^* [Mpa]	247	239
ε_A^*	0.052	0.05
L_A [mm]	140.3	197.5
L_M [mm]	145	203.7
F_F [N]	50	30
L_0 [mm]	139.5	196.6
F_A^* [N]	313.9	304.1
F_M^* [N]	172.1	156.8
K_T [N/mm]	30	23.8
K_S [N/mm]	19.4	18.9
Preload [mm]	8.9	8.3

The thickness distribution and the deformed shape are reported in Fig. 16, the maximum stress is close to 22 MPa and the average deviation of the deformed profile from the desired one is 6 mm, with a maximum discrepancy of 22 mm.

The NiTi actuators are then designed according to the described procedure and to the selected values of the frame parameters F_F, L_A, L_M, σ_A^*, obtaining the data in Table 2 and the characteristics in Fig. 17.

In this case the stress σ_A^* is appropriately set so that the spring stiffness is close to 19 N/mm, matching that of the compression spring selected for realizing the actuator.

As visible in Figs. 13 and 16, the predicted deformations of the frame indicate a profile curvature more pronounced than that of the M27 airfoil in the area of the trailing edge, for both the frame schemes evaluated. This is attributed to the position chosen for the rear actuator, common to both frames, suggesting that a different placement of the rear actuator could be more effective of the beams network topology in inducing frame deformations more adherent to the M27 airfoil shape.

Instead, the deformations of the leading edge area are more accurate for the frame #1 than for #2, despite the load has again the same direction, indicating that in this case the frame topology plays a significant role in determining the deformed shape.

More generally, both loads directions and magnitude could be used as variables within the G.A., together with the thickness set and, eventually, to the position of some or all the internal nodes.

In the spirit of the demonstrative character of this study, no further design optimization will be carried

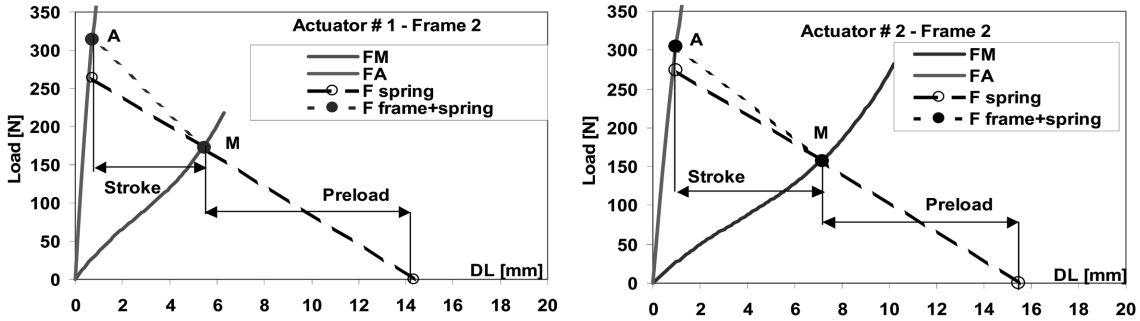

Fig. 17 Actuators diagrams for frame # 2

out for achieving a more accurate reproduction of the desired profile. The remaining part of this paper is devoted to verifying by experiments if the predictions of the described procedure are reasonably accurate.

6. Demonstrator testing

Each actuator is manufactured according to the scheme of Fig. 9 and the parameters reported in Table 2. Two screw registers for tuning the spring preload are added, as in Fig. 18, while the wing rib is c.n.c. machined from a plate of Nylon 66, 21 mm thick. Four attachments are provided for placing the two actuators in the selected positions.

The assembled wing rib is then tested by feeding the wires with direct current and acquiring the images of Fig. 19 for evaluating both the deformed and undeformed states.

Black dots are marked along the wing rib profile and their coordinates are read by image analysis techniques, so the experimental deformed shape is acquired for comparison with the deformed frame as it is predicted by the genetic/structural analysis.

In Fig. 20 are reported the two deformed profiles, together with the plots of their distance measured normally to the chord, at fixed measurement stations along the chord.

Positive values of this distance indicate that the experimental profile is higher than the numerical profile.

The discrepancy between expected and measured displacements is greater at the trailing edge than elsewhere along the airfoil, most probably because the beams in this area are too short to be correctly

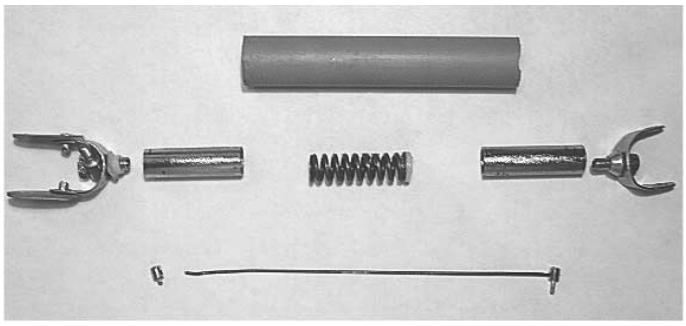

Fig. 18 Actuator components

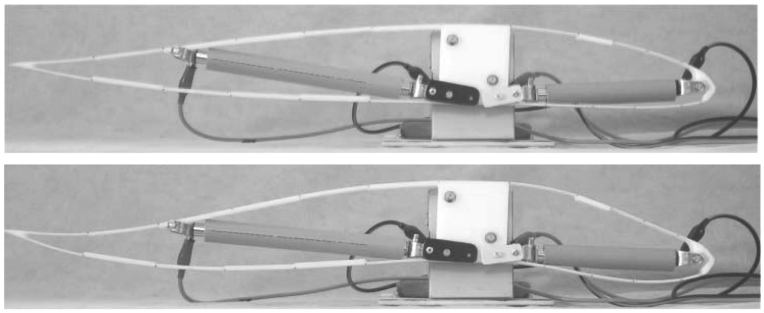

Fig. 19 Undeformed and deformed configurations of the wing rib

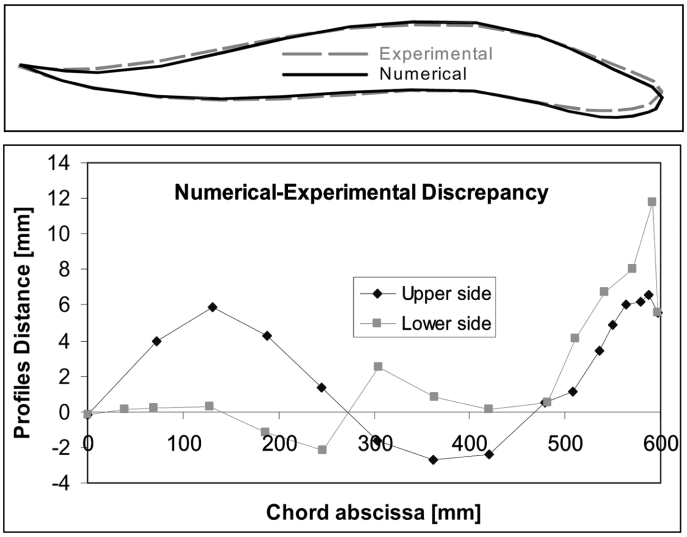

Fig. 20 Deformed wing rib from numerical predictions and from experiments

simulated by the Euler beams theory and the columns theory. In fact, when the length of a beam is comparable to the larger dimension of its cross section, the Timoshenko formulation becomes essential for the accuracy in predicting displacements and finite elements analyses should be carried out. Also the geometrical nonlinearities arising from large displacements should be accounted for in such a compliant structure, while here complete linearity is assumed.

Despite these considerations, the maximum absolute error of 12 mm is still a small percentage (2%) of the wing chord, and the overall shape of the profile acquired in the deformed state is definitely close to the predicted approximation of the M27 airfoil.

The studied transformation of the wing shape is suitable for slow and intermittent maneuvers like setting the wing shape in different phases of the flight (take off, cruise at different weather/speed conditions, landing, etc.); in fact, the response of this kind of systems to the input electric current is not sufficiently rapid to be used for the sharp and quick maneuver requirements typical of in-flight handling. Faster response of the actuators can be achieved by controlling the feeding current with closed loop systems, but in this way the energetic efficiency of the system quickly deteriorates.

Other important aspects like the aeroelastic fluid-structure interaction and fatigue-damage of materials should be taken into account for the detailed structural design of a wing but, in principle, the methodology presented in this paper applies to the design of large scale smart wings and this work can be intended as a conceptual approach to the problem.

7. Conclusions

Continuously deforming wings constitute the more efficient mean of generating the lift and the control forces necessary to handle a flight vehicle, as the flight of birds suggests. The study presented here is aimed at obtaining such a type of morphing wing, capable of switching between two different airfoil configurations without discontinuities and abrupt variations of the wing surface.

The adoption of shape memory alloys as a mean of actuation is encouraged by the good energy/mass

ratio typical of the actuators based on these metals.

A satisfactory degree of accuracy is achieved in predicting both the structure behavior and the performance of the shape memory alloy actuators, despite in-depth analyses (large displacements FEA, variability of the structure topology and loads within the G.A., etc.) were not carried out.

The strategy implemented by coupling structural analysis with genetic algorithms confirmed itself as a promising tool for designing compliant wing structures whose mechanical responses have to be tailored for matching the requirements of SMA-based actuators.

References

Araujo, C.J. and Gonzalez, C.H. (2007), "On two-step strain–temperature behavior in Cu–Zn–Al shape memory alloy wire actuators", *Smart Mater. Struct*., **16**, 884-890.

Auricchio, F. and Sacco, E. (1999), "A temperature-dependent beam for shape-memory alloys: costitutive modelling, finite-element implementation and numerical simulations", *Comput. Methods Appl. M.,* **174**, 171-190.

Azadi, B., Rajapakse, R.K.N.D. and Majier, D.M. (2006), "One-dimensional thermomechanical model for dynamic pseudoelastic response of shape memory alloys", *Smart Mater. Struct*., **15**, 996-1008.

Bein, T.H., Hanselka, H. and Breitbach, E. (2000), "An adaptive spoiler to control the transonic shock", *Smart Mater. Struct*., **9**, 141-148.

Brinson, L.C. (1993), "One-dimensional constitutive behavior of shape memory alloys: thermomechanical derivation with non-constant material functions and redefined martensite internal variable", *J. Intel. Mat. Syst. Str.,* **4**, 229-242.

Brinson, L.C. and Huang, M.S. (1996), "Simplifications and Comparisons of shape memory alloy constitutive models", *J. Intel. Mat. Syst. Str.,* **7**, 108-114.

Brocca, M., Brinson, L.C. and Bazant, Z.P. (2002), "Three-dimensional constitutive model for shape memory alloys based on microplane model", *J. Mech. Phys. Solids*, **50**, 1051-1077.

Campanile, F., Seack, O. and Sachau, D. (2000), "The belt-rib concept for variable-camber airfoils: recent developments", *SPIE Symposium on Smart Structures and Materials*.

Campanile, L.F. and Anders, S. (2005), "Aerodynamic and aeroelastic amplification in adaptive belt-rib airfoils", *Aerosp. Sci. Technol*., **9**, 55-63.

Drela, M. (2001), *XFOIL v.6.9 User guide*, MIT Aero & Astro Harold Youngren Aerocraft, Inc.

Ezley, D.M., Sofla, Y.N. and Wadley, H.N.G. (2005), "A shape memory based multifunctional structural actuator panel", *Int. J. Solids Struct.*, **42**, 1943-1955.

Flemings, G.A. and Burner, A.W. (1999), "Deformation measurements of smart aerodynamic surfaces", *44th SPIE Int. Symposyum on Optical Science*, Engineering and Instrumentation.

Gandhi, F. and Anusonti-Inthra, P. (2008), "Skin design studies for variable camber morphing airfoils", *Smart Mater. Struct.,* **17**, 15-25.

Garner, L.J., Wilson, L.N., Lagoudas, D.C. and Rediniotis, O.K. (2000), "Development of a shape memory alloy actuated biomimetic vehicle", *Smart Mater. Struct.*, **9**, 673-783.

Govindjee, S. and Garrett, J.H. (2000), "A computational model for shape memory alloys", *Int. J. Solids Struct.*, **37**, 735-760.

Huang, W. (2002), "On the selection of shape memory alloys for actuators", *Mater. Design*, **23**, 11-19.

Icardi, U. (2001), "Large bending actuator made with SMA contractile wires: theory, numerical simulation and experiments", *Compos. Part B*, **32**, 259-267.

Kato, H., Inagaki, N. and Sasaki, K. (2004), "A one-dimensionale modelling of constrained shape memory effect", *Acta Mater*., **52**, 3375-3382.

Lu, K.J. and Kota, S. (2002), "Compliant mechanism synthesis for shape-change applications: preliminary results", *SPIE Conf. on Smart Structures and Materials*, **4693**, 161-172.

Lu, Z.K. and Weng, G.J. (1997), "Martensitic transformations and stress-strain relations of shape-memory alloys", *J. Mech. Phys. Solids*, **45**, 1905-1928.

Lim, S.M., Lee, S.K., Park, H.C., Yoon, K.J. and Goo, N. S. (2005), "Design and demonstration of a biomimetic wing section using a lightweight piezo-composite actuator (LIPCA)", *Smart Mater. Struct*., **14**, 496-503.
Mirone, G. (2007), "Design and demonstrators testing of adaptive airfoils and hingeless wings actuated by shape memory alloy wires", *Smart Struct. Syst*., 3.
Monner, H.P. (2001), "Realization of an optimized wing camber by using formvariable flap structures", *Aerosp. Sci. Technol*., **5**, 445-455.
Neal, D.A., Good, M.G., Johnston, C.O., Robertshaw, H.H., Mason, W.H. and Inman, D.J. (2004), "Design and wind-tunnel analysis of a fully adaptive aircraft configuration", AIAA paper, 2004-1727.
Nemat-Nasser, S. and Guo, W.G. (2006), "Superelastic and cyclic response of NiTi SMA at various strain rates and temperatures", *Mech. Mater*., **38**, 463-474.
Pettit, G.W., Robertshaw, H.H. and Inman, D.J. (2001), "Morphing wings for unmanned aircraft", *Smart Materials Bulletin*, 11.
Raja, S., Pashilkar, A.A., Sreedeep, R. and Kamesh, J.V. (2006), "Flutter control of a composite plate with piezoelectric multilayered actuators", *Aerosp. Sci. Technol*., **10**, 435-441.
Shili, L., Wenjie, G. and Shujun, L. (2008), "Optimal design of compliant trailing edge for shape changing", *Chinese J. Aeronautics*, **21**, 187-192.
Syaifuddin, M., Park, H.C. and Goo, N.S. (2006), "Design and evaluation of a LIPCA-actuated flapping device", *Smart Mater. Struct*., **15**, 1225-1230.
Schmitt, L.M. (2001), "Theory of genetic algorithms", *Theor. Comput. Sci*., **259**, 1-61.
Song, G. and Ma, N. (2007), "Robust control of a shape memory alloy wire actuated flap", *Smart Mater. Struct.*, **16**, N51-N57.
Stanewsky, E. (2000), "Aerodynamic benefits of adaptive wing technology", *Aerosp. Sci. Technol*., **4**, 439-452.
Strelec, J.K., Lagoudas, D.C., Khan, M.A. and Yen, J. (2003), "Design and implementation of a shape memory alloy actuated reconfigurable airfoil", *J. Intel. Mat. Syst. Str.*, **14**, 257-273.
Strelec, J.K. and Lagoudas, D.C. (2002), "Fabrication and testing of a shape memory alloy actuated reconfigurable wing", *9th SPIE Symposium on Smart Structures and Materials*, **4701**, 267-280.
Talay, T.A. (1975), *Introduction to the aerodynamics of flight*, Langley Research Centre, NASA SP367.
Tanaka, K., Nishimura, F., Hayashi, T., Tobushi, H. and Lexcellent, C. (1995), "Phenomenological analysis on subloops and cyclic behaviour in shape memory alloys under mechanical and/or thermal loads", *Mech. Mater*., **19**, 281-292.
Tanaka, N. and Sanada, T. (2007), "Modal control of a rectangular plate using smart sensors and smart actuators", *Smart Mater. Struct*., **16**, 36-46.
Trochu, F., Sacépé, N., Volkov, O. and Turenne, S. (1999), "Characterization of NiTi shape memory alloys using dual kriging interpolation", *Mater. Sci. Eng*., **A273**, 395-399.
Tzou, H.S., Ye, R. and Ding, J.H. (2001), "A new x-actuator design for dual bending/twisting control of wings", *J. Sound Vib.*, **241**(2), 271-281.
Van Blyenburgh, P. (1999), "UAVs: an overview", *Air Space Europe*, **1**, 43-47.
Vose, M.D. (1999), *The simple genetic algorithm: foundations and theory*, MIT Press, Cambridge, MA.
Vos, R., Barrett, R., de Breuker, R. and Tiso, P. (2007), "Post-buckled precompressed elements: a new class of control actuators for morphing wing UAVs", *Smart Mater. Struct*., **16**, 919-926.
Waisman, H. and Abramovich, H. (2004), "Open-loop flutter analysis of a composite UAV model using the active stiffening effect", *Finite Elem. Anal. Des*., **40**, 1283-1295.
Whitley, D. (1994), "A genetic algorithm tutorial", *Stat. Comput*., **4**, 65-85.

FC